

High resolution on-chip spectroscopy based on miniaturized microdonut resonators

Zhixuan Xia, Ali Asghar Eftekhari, Mohammad Soltani, Babak Momeni, Qing Li, Maysamreza Chamanzar, Siva Yegnanarayanan, and Ali Adibi *

School of Electrical and Computer Engineering, Georgia Institute of Technology, 777 Atlantic Drive NW, Atlanta, Georgia 30332, USA

*adibi@ece.gatech.edu

Abstract: We experimentally demonstrate a high resolution integrated spectrometer on silicon on insulator (SOI) substrate using a large-scale array of microdonut resonators. Through top-view imaging and processing, the measured spectral response of the spectrometer shows a linewidth of ~ 0.6 nm with an operating bandwidth of ~ 50 nm. This high resolution and bandwidth is achieved in a compact size using miniaturized microdonut resonators (radius $\sim 2\mu\text{m}$) with a high quality factor, single-mode operation, and a large free spectral range. The microspectrometer is realized using silicon process compatible fabrication and has a great potential as a high-resolution, large dynamic range, light-weight, compact, high-speed, and versatile microspectrometer.

©2011 Optical Society of America

OCIS codes: (130.3120) Integrated optics devices; (230.5750) Resonators; (300.6190) Spectrometers.

References and links

1. J. Hubner, A. M. Jorgensen, T. A. Anhoj, and D. A. Zauner, "Integrated optical systems for lab-on-chip applications," *Proc. SPIE* **5728**, 269–277 (2005).
2. J. Xu, D. Suarez, and D. S. Gottfried, "Detection of avian influenza virus using an interferometric biosensor," *Anal. Bioanal. Chem.* **389**(4), 1193–1199 (2007).
3. B. Momeni, S. Yegnanarayanan, M. Soltani, A. A. Eftekhari, E. Shah Hosseini, and A. Adibi, "Silicon nanophotonic devices for integrated sensing," *J. Nanophoton.* **3**(1), 031001 (2009).
4. T. Fukazawa, F. Ohno, and T. Baba, "Very compact arrayed-waveguide-grating demultiplexer using Si photonic wire waveguides," *Jpn. J. Appl. Phys.* **43**(No. 5B), L673–L675 (2004).
5. K. Kodate and Y. Komai, "Compact spectroscopic sensor using an arrayed waveguide grating," *J. Opt. A, Pure Appl. Opt.* **10**(4), 044011 (2008).
6. S. Janz, A. Balakrishnan, S. Charbonneau, P. Cheben, M. Cloutier, A. Delage, K. Dossou, L. Erickson, M. Gao, P. A. Krug, B. Lamontagne, M. Packirisamy, M. Pearson, and D.-X. Xu, "Planar waveguide echelle gratings in silica-on-silicon," *IEEE Photon. Technol. Lett.* **16**(2), 503–505 (2004).
7. J. Song and N. Zhu, "Design and fabrication of compact etched diffraction grating demultiplexers based on α -Si nanowire technology," *Electron. Lett.* **44**(13), 816–818 (2008).
8. F. Horst, W. M. J. Green, B. J. Offrein, and Y. Vlasov, "Echelle grating WDM demultiplexers in SOI technology, based on a design with two stigmatic points," *Proc. SPIE* **6996**, 69960R, 69960R-8 (2008).
9. B. Momeni, M. Chamanzar, E. Shah Hosseini, M. Askari, M. Soltani, and A. Adibi, "Strong angular dispersion using higher bands of planar silicon photonic crystals," *Opt. Express* **16**(18), 14213–14220 (2008).
10. B. Momeni, E. S. Hosseini, M. Askari, M. Soltani, and A. Adibi, "Integrated photonic crystal spectrometers for sensing applications," *Opt. Commun.* **282**(15), 3168–3171 (2009).
11. B. B. C. Kyotoku, L. Chen, and M. Lipson, "Sub-nm resolution cavity enhanced microspectrometer," *Opt. Express* **18**(1), 102–107 (2010).
12. R. F. Wolffenbuttel, "State-of-the-Art in integrated optical microspectrometers," *IEEE Trans. Instrum. Meas.* **53**(1), 197–202 (2004).
13. S.-W. Wang, C. Xia, X. Chen, W. Lu, M. Li, H. Wang, W. Zheng, and T. Zhang, "Concept of a high-resolution miniature spectrometer using an integrated filter array," *Opt. Lett.* **32**(6), 632–634 (2007).
14. R. G. DeCorby, N. Ponnampalam, E. Epp, T. Allen, and J. N. McMullin, "Chip-scale spectrometry based on tapered hollow Bragg waveguides," *Opt. Express* **17**(19), 16632–16645 (2009).
15. M. Soltani, Q. Li, S. Yegnanarayanan, B. Momeni, A. A. Eftekhari, and A. Adibi, "Large-scale array of small high-Q microdisk resonators for on-chip spectral analysis," in *Proceedings of IEEE LEOS Annual Meeting Conference* (Institute of Electrical and Electronics Engineers, Belek-Antalya, Turkey, 2009), pp. 703–704.

16. M. Soltani, Q. Li, S. Yegnanarayanan, and A. Adibi, "Toward ultimate miniaturization of high Q silicon traveling-wave microresonators," *Opt. Express* **18**(19), 19541–19557 (2010).
 17. Q. Xu, D. Fattal, and R. G. Beausoleil, "Silicon microring resonators with 1.5-microm radius," *Opt. Express* **16**(6), 4309–4315 (2008).
 18. Q. Li, M. Soltani, S. Yegnanarayanan, and A. Adibi, "Design and demonstration of compact, wide bandwidth coupled-resonator filters on a silicon-on-insulator platform," *Opt. Express* **17**(4), 2247–2254 (2009).
 19. J. Schrauwen, D. Van Thourhout, and R. Baets, "Trimming of silicon ring resonator by electron beam induced compaction and strain," *Opt. Express* **16**(6), 3738–3743 (2008).
 20. C. W. Holzwarth, T. Barwicz, M. A. Popovic, P. T. Rakich, E. P. Ippen, F. X. Kartner, and H. I. Smith, "Accurate resonant frequency spacing of microring filters without postfabrication trimming," *J. Vac. Sci. Technol. B* **24**(6), 3244–3247 (2006).
 21. R. Soref, "Mid-infrared photonics in silicon and germanium," *Nat. Photonics* **4**(8), 495–497 (2010).
 22. D. K. Sparacin, C. Y. Hong, L. C. Kimerling, J. Michel, J. P. Lock, and K. K. Gleason, "Trimming of microring resonators by photooxidation of a plasma-polymerized organosilane cladding material," *Opt. Lett.* **30**(17), 2251–2253 (2005).
 23. C. J. Chen, C. A. Husko, I. Meric, K. L. Shepard, C. W. Wong, W. M. J. Green, Y. A. Vlasov, and S. Assefa, "Deterministic tuning of slow-light in photonic-crystal waveguides through the C and L bands by atomic layer deposition," *Appl. Phys. Lett.* **96**(8), 081107 (2010).
 24. C.-C. Chang and H.-N. Lee, "On the estimation of target spectrum for filter-array based spectrometers," *Opt. Express* **16**(2), 1056–1061 (2008).
-

1. Introduction

Integrated photonic sensors have received considerable attention in recent years due to their inherent advantages, including high sensitivity, low cost of fabrication, versatility, compactness, and low power consumption [1–3]. The progress of integrated photonic sensors has reached the point that requires integration of different system components together for an overall efficient sensing system. One of the major building blocks for such lab-on-chip sensing systems is an integrated spectrometer that enables on-chip spectral analysis.

Motivated by this demand, there has been significant progress in the realization of integrated microspectrometers in different configurations such as arrayed-waveguide gratings [4,5], grating spectrometers [6–8], superprism-based spectrometers [9,10], and the recently demonstrated diffractive grating spectrometer combined with the thermally tunable microring resonators [11]. However, the main challenge of the integrated spectrometers that rely on dispersive components is the trade-off between the resolution and the size of the structure [12]. As an alternative, a filter array with Fabry-Perot cavities has been proposed to provide high spectral resolution (1.7 – 3.8 nm) in the near infrared region [13]. In this approach, different spectral components of the incoming signal are individually captured by their corresponding filters with a varying vertical cavity length obtained by multiple film deposition steps. An array of detectors is used to measure the output of all filtered spectral component simultaneously and sent the data to an electronic processing device in real time. This method, without any moving parts and conventional dispersive structures, enables parallel spectral processing in a very short time, which is critical for a variety of biological and biomedical applications. However, the aforementioned Fabry-Perot filter array suffers from the complexity of fabricating highly reflective and parallel mirrors with a series of different cavity lengths, and its resolution is limited by the available reflectance of the cavity mirrors. More importantly, the trade-off between the resolution and free spectral range (FSR) of the Fabry-Perot cavity is a limiting factor for applications requiring large operating bandwidth [14].

In this paper, we propose a new microspectrometer architecture based on a large array of compact microdonut resonators to address the challenges of existing on-chip spectrometers. The key building element used to construct the microspectrometer is a miniaturized microdonut resonator [15,16] offering single mode operation with a high quality factor (Q) and a large FSR.

The proposed spectrometer employs a filter array of microdonut resonators, which is coupled to an input bus waveguide, as is schematically shown in Fig. 1(a). The microdonut resonators are carefully designed such that each of the resonators only taps a small portion of

the incoming spectrum that overlaps with its resonance lineshape, as is shown in Fig. 1(b). In this architecture, each resonator corresponds to a unique spectral channel. The input signal power in each spectral channel can be coupled to a separate output waveguide or directly coupled out of plane through the resonator. By imaging the output power of different spectral channels using a detector array or a charge-coupled detector (CCD) chip on top of the resonator array device, the entire input signal spectrum can be measured in real time. This on-chip spectrometer can be fabricated using CMOS-compatible manufacturing techniques and thus can be readily integrated with integrated sensors, optoelectronics, microelectronics and microfluidic channels. This enables the realization of a system-on-a-chip suitable for several applications in biological, chemical, medical, and pharmaceutical industries. The rest of the paper is organized as follows: major properties of microdonut resonators are presented in Section 2. Section 3 is dedicated to the design and fabrication of the on-chip spectrometers. The experimental results are presented and discussed in Sections 4 and 5, respectively. Final conclusions are made in Section 6.

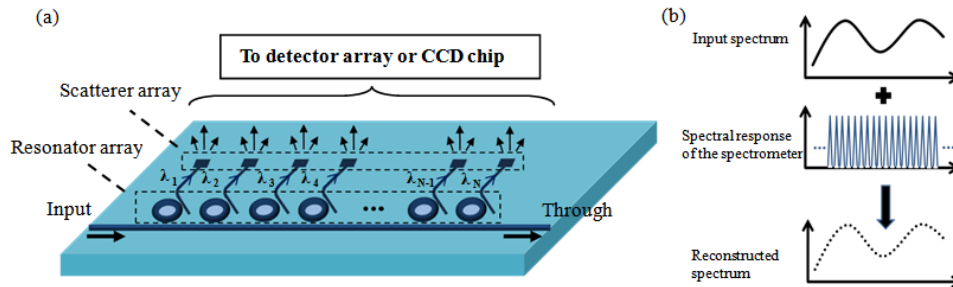


Fig. 1. (a) Configuration of the resonator-array spectrometer: a 1-D array of small microdonut resonators samples different spectral channels of the input signal propagating in the bus waveguide. Each spectral channel is coupled by one resonator to a corresponding drop waveguide and then scattered out-of-plane in an arrangement prepared for a detector array on top of the structure. (b) Working principle of the resonator-array spectrometer: the unknown input spectrum is sampled by the series of resonances provided by the resonators in the array followed by data processing to obtain the reconstructed spectrum of the input signal.

2. Microdonut resonators

To simultaneously achieve a high Q and a large FSR, a miniaturized microdonut resonator is used [16]. As shown in Fig. 2(a), a microdonut resonator is essentially a microdisk with an inner hole perforated at the center. In this configuration, the fundamental radial mode of the resonator is mostly confined around the outer perimeter of the microdonut (see Fig. 2(c)) while the higher-order radial modes are pushed into the leaky zone, leading to a single-mode operation. The major difference between the microdonut resonator and the miniaturized microring resonator [16] is that by adjusting the radius of the inner hole, the fundamental radial mode of a microdonut resonator interacts only with the outer sidewall of the resonator, while such a mode always interacts with two sidewalls in microring resonators. Consequently, a higher quality factor for the fundamental mode is expected when using microdonut resonators. Figure 2(a) shows the scanning electron microscope (SEM) image of an add/drop filter based on the compact microdonut resonator with a radius of $\sim 2 \mu\text{m}$ and an oxide cladding. A linewidth of $\sim 50 \text{ pm}$ is measured from the drop port transmission for TE polarization (i.e., electric field confined in the plane of the device) (see Fig. 2(b)), leading to a loaded Q (Q_L) of $\sim 30,000$ (corresponding to an intrinsic Q of $Q_i \sim 80,000$). This Q_i is twice that achieved with microring resonator with a similar diameter [17]. Figure 2(c) confirms the single-mode operation of the miniaturized microdonut resonator with an FSR of $\sim 57 \text{ nm}$.

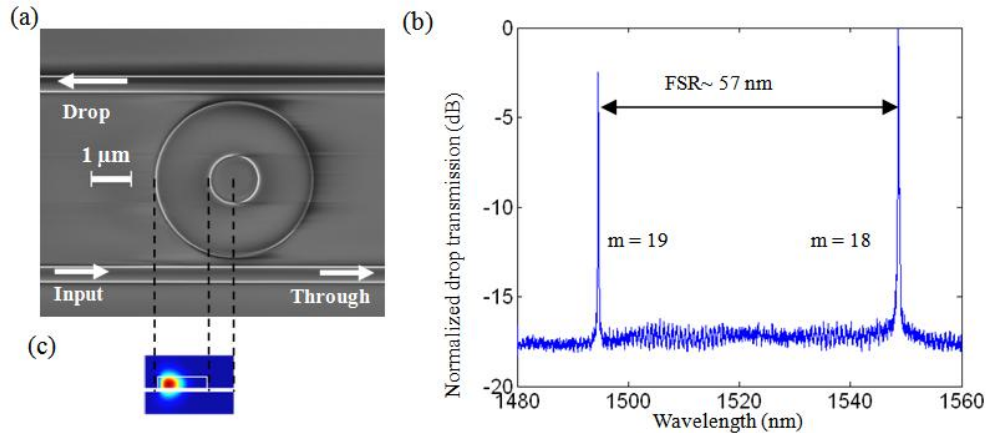


Fig. 2. (a) The SEM image of a microdonut resonator in an add/drop configuration: the width and thickness for both waveguides are 400 nm and 230 nm, respectively. The outer radius of the microdonut resonator is $r_{\text{out}} = 1.97 \mu\text{m}$ with a center hole with a radius of $r_{\text{in}} = 0.6 \mu\text{m}$. The gap between the waveguide and the resonator is 240 nm. The microdonut resonator has a 2 μm thick oxide cladding layer. (b) The experimental transmission spectrum of the drop port of the resonator in Part (a) for TE polarization showing two resonances belonging to the fundamental radial modes with different azimuth mode numbers (m) specified in the figure. The measured linewidth is $\sim 50 \text{ pm}$ and the FSR is $\sim 57 \text{ nm}$. (c) Simulated fundamental TE mode profile of the microdonut resonator with $m = 18$, indicating a majority of light is confined at the outer perimeter of the resonator.

By engineering the geometry of the microdonut resonator (i.e., the outer and inner radii), its resonance wavelength can be adjusted. Because of the small mode volume and high field intensity of the resonant mode at the outer perimeter (see Fig. 2(c)), the resonance is very sensitive to the variations of the outer radius. Simulations using three-dimensional finite element method (3D FEM) show that every 1 nm variation in the outer radius of a microdonut with a radius of $r_{\text{out}} \sim 2 \mu\text{m}$ and a thickness of 230 nm corresponds to a 0.6 nm change in its resonance wavelength near 1550 nm. Meanwhile, the fine-tuning of the resonance (better than 10 pm wavelength accuracy) can be achieved by adjusting the inner radius of the microdonut resonator. The spectral linewidth of the resonance (and thus its Q_L) is controlled by engineering the coupling between the bus waveguide and the microdonut resonator. Therefore, combined with the high Q_i and large FSR, the ability to independently tune the resonance location and spectral resolution makes the microdonut resonator an excellent building-block device to construct a large-scale resonator array suitable for on-chip spectroscopy.

3. Design and fabrication of on-chip spectrometer with microdonut resonators

The micrograph of an on-chip resonator-array spectrometer composed of an array of resonators side coupled to a bus waveguide is shown in Fig. 3(a). The spectrometer is designed to work with TE polarization. The input light signal (with a target spectrum to be detected) is coupled through the bus waveguide from the lower left in Fig. 3(a). Each of the resonators filters the input signal in a narrow spectral window and sends it via its corresponding side coupled drop waveguide to a scatterer located at the end of the drop waveguide. In this architecture, each resonator, its drop waveguide and the corresponding scatterer describe a spectral channel that measures a unique spectral portion of the target spectrum. The response of each spectral channel is indicated by the out-of-plane radiation from the scatterer of that channel, and it is measured by imaging the signal from the scatterer array onto a detector array, as shown in Figs. 3(b)–3(d).

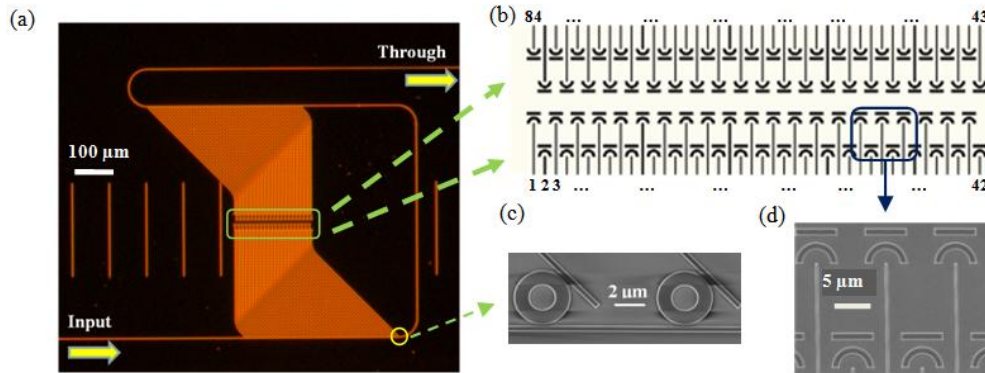


Fig. 3. (a) Micrograph of the proposed spectrometer: incoming light is coupled to the structure through the input waveguide on the lower left of the figure. Each of the resonators is side coupled to the input waveguide from one side and to a drop waveguide from the other side to filter the input signal in a narrow spectral window. The filtered signal is scattered out of the chip by a scatterer at the end of the drop waveguide. (b) The 2-D array of the scatterers with channel numbers labeled. (c) The SEM image of two microdonut resonators coupled to the input waveguide and their corresponding drop waveguides. The center-to-center distance between the two adjacent microdonut resonators is $10.0\ \mu\text{m}$, the gap between the microdonut and each waveguide is $130\ \text{nm}$, and the widths of the input and bus waveguides are $400\ \text{nm}$. (d) The SEM image of a portion of the 2-D array of the scatterers.

The number of the resonators in the array and their resonance wavelengths and linewidths are adjusted to cover one full FSR of a single resonator. Tuning of the resonance wavelength is achieved by varying the outer radius (initially $\sim 2\ \mu\text{m}$) with $1\ \text{nm}$ steps, while keeping the inner radius fixed at $0.9\ \mu\text{m}$ to ensure the single-mode operation at around $1550\ \text{nm}$. This leads to a $\sim 0.6\ \text{nm}$ increment in the resonance wavelengths of adjacent spectral channels as calculated from 3D FEM in the COMSOL environment. Considering an FSR of $\sim 60\ \text{nm}$, the operating bandwidth is designed to be $\sim 50\ \text{nm}$ to avoid the interference of resonances from different azimuthal modes. A total number of 84 microdonut resonators are needed to cover the operating bandwidth without too much overlap among the neighboring resonances. The outer radii of the resonators are chosen ranging from $1.950\ \mu\text{m}$ to $2.033\ \mu\text{m}$. The resonance linewidth of the resonators is set to be $\sim 0.3\ \text{nm}$, corresponding to a Q of $Q_L \sim 5000$. This linewidth is achieved by setting the gap size between the resonators and the bus waveguide to $130\ \text{nm}$. According to 3D FEM calculations, the effective coupling Q of Q_C is $\sim 10,000$. Considering the two coupling regions (corresponding to the input and the drop ports) as well as the much higher intrinsic quality factor Q_i of the microdonut resonator, the estimated loaded Q_L would be ~ 5000 ($1/Q_L = 2/Q_C + 1/Q_i \approx 2/Q_C$). In this configuration, the spectrometer samples the incoming target spectrum with 84 sharp Lorentzian-like peaks with a constant spacing of $\sim 0.6\ \text{nm}$ as schematically shown in Fig. 1(a). The width of the straight waveguide is chosen to be $400\ \text{nm}$ to ensure single mode operation at the wavelength region of $1500\ \text{nm}$ - $1640\ \text{nm}$. The drop waveguides are designed to uniformly and efficiently transmit the spectrum channel light energy to the scatterers. To ensure that all the scatterers fall within the field-of-view of the CCD, the drop waveguides and their scatterers are packed in the center (from the top and bottom) of the device as shown in Figs. 3(a) and 3(b). This leads to a small size for the 84-element scatterers array ($\sim 200\ \mu\text{m}$ by $50\ \mu\text{m}$ in total) that can be readily imaged within the field-of-view of the CCD using a $20\times$ objective lens. The scatterers are placed in a 2D array, where the scatterers with different parities are located in different rows, as shown in Fig. 3(b). Therefore, one scatterer of a certain channel is always placed in a different row from both of its immediate neighbor channels. This helps to lower the crosstalk

among the neighboring channels and to easily identify the channel number in the spectrum estimation.

The spectrometer structure was fabricated on an SOI wafer with a Si layer thickness of 230 nm on top of a 1 μm buried oxide layer. The device was patterned using a JBX-9300FS electron beam lithography (EBL) system with 6% dilute hydrogen silsesquioxane (HSQ) negative electron resist and etched in an inductively-coupled plasma etching system with Cl_2 chemistry. The details of the fabrication process have been reported elsewhere [18]. A 1 μm thick layer of SiO_2 is subsequently deposited on top of the structure using plasma enhanced chemical vapor deposition (PECVD) as the cladding and passivation layer.

4. Experimental results

The characterization of the spectrometer is first conducted by coupling light from a tunable laser (81640A, Agilent Technologies) to the input bus waveguide via a tapered fiber. The output power of the through port is collected by a photodetector (Thorlabs PDB 150C) through another tapered fiber. The measured transmission spectrum from the through port (see Fig. 3(a)) waveguide is shown in Fig. 4(a). The FSR of the smallest microdonut resonator (outer radius $\sim 1.950 \mu\text{m}$) is measured to be $\sim 60 \text{ nm}$, which corresponds to the resonance wavelength spacing between the azimuthal modes $m = 17$ and $m = 18$ of the fundamental radial TE mode. The resonances of the resonator array densely fill up the FSR, indicating the capability of sampling a target spectrum. However, among the total 84 microdonut resonators in the array, three of the designed resonances are missing and a total of 81 resonances are observed in both the through port transmission and the top view IR camera imaging that will be discussed later. For the functioning 81 channels, the typical value of the measured loaded Q is $Q_L \sim 5000$, which is in good agreement with the original design. Figure 4(b) plots the measured resonances of the resonator array obtained directly from Fig. 4(a), showing the channel-to-channel uniformity of the 81 resonances. The measured resonance spacing varies between $\sim 0.2 \text{ nm}$ and $\sim 1.0 \text{ nm}$, due to the high sensitivity of the resonance wavelength to changes in the outer radius of the microdonut resonators, the imperfections in the device fabrication, and possibly the thickness variation of the wafer. The solid line and the inset formula in Fig. 4(b) show the linear regression model obtained by the measured data points. The shift of the measured resonances from their projected values with the linear fitting model is depicted by the standard error of $\sim 0.400 \text{ nm}$. The good linearity with an average resonance spacing of $\sim 0.636 \text{ nm}$ agrees well with the design value of $\sim 0.6 \text{ nm}$.

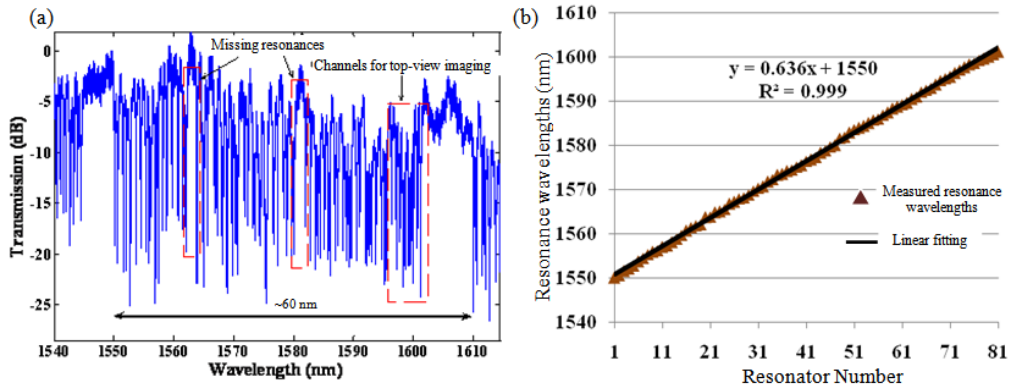


Fig. 4. (a) Transmission spectrum measured from the through port waveguide, indicating an FSR of $\sim 60 \text{ nm}$. (b) Plot of the measured resonance wavelengths of different resonators (vertical axis, y) versus their resonator number in the resonator array (horizontal axis, x , $x = 1-81$, which only include the working 81 resonators with observed resonances). The inset formula shows the linear functions fitted to the measured resonance wavelengths. The correlation between the measured data points and the fitted linear model (R^2) is 0.999.

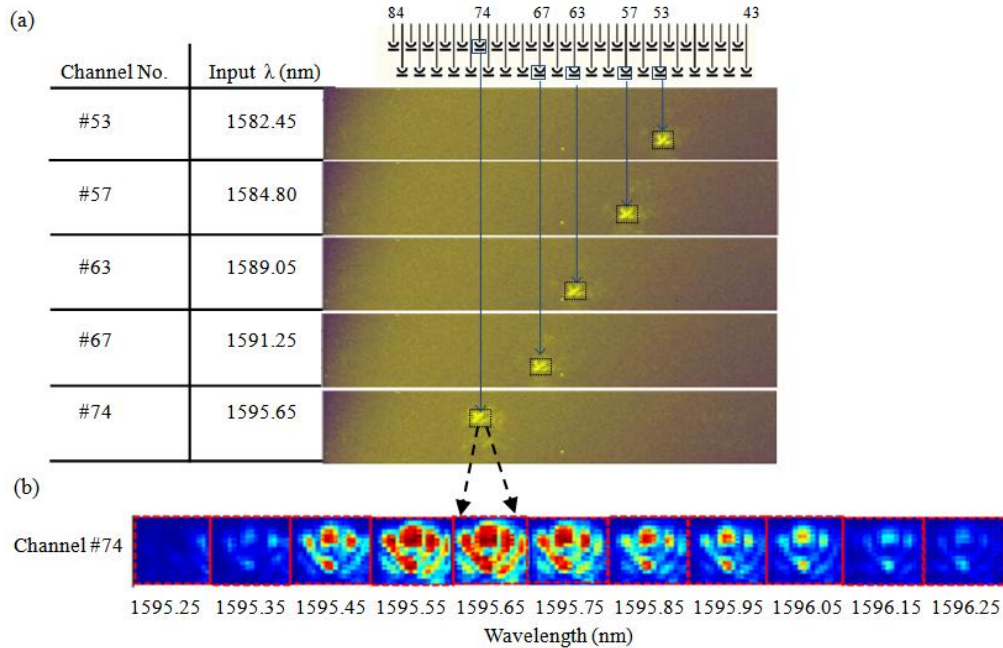


Fig. 5. (a) Real time images captured by the IR camera showing different channel responses at five different input wavelengths (nm): 1582.45, 1584.80, 1589.05, 1591.25, and 1595.65, when the input spectrum falls within channel numbers 53, 57, 63, 67, 74, respectively. Note that this figure only shows the upper portion of the scatterer array. (b) Post-processed light pattern scattered by channel #74 at different input wavelengths around its resonance.

The response of the spectrometer is then characterized by capturing the out-of-plane radiation of the scatterer array with an IR camera (Sensors Unlimited SU128-1.7RT, 128 by 128 pixels with pixel size of $60 \mu\text{m}^2$), while varying the input wavelength using a tunable laser (81640A, Agilent Technologies) at $500 \mu\text{w}$ output power. During the full wavelength scan over one FSR from 1550 nm to 1610 nm at a step of 0.05 nm, 81 out of the total 84 scatterers turned on (with strong out-of-plane radiation observed in the real time imaging). The remaining three resonators are not observed either in the transmission or in the out of plane image. With the transmission spectrum and the location of the scatterers that failed to turn on, the defective channels were identified with resonator numbers #20, #21, and #50. This can be due to the large shift of the resonance of these three channels as a result of fabrication imperfection causing them to overlap with adjacent resonances; it can also be due to unwanted large imperfection resulting in low intrinsic Q s for these three resonators. Figure 5(a) shows the top images of the upper portion of the scatterer array at different input wavelengths, corresponding to the designed channels #43 - #84. The top image of the scatterer corresponding to the spectral channel #74 for different input wavelengths is shown in Fig. 5(b). We can clearly see the total scattered power peaks at 1595.65 nm, which corresponds to the assigned center resonance wavelength for this channel. Good extinction ratio is also observed within ~ 0.5 nm from the center wavelength as shown in Fig. 5(b). By integrating the amplitudes of the CCD pixels for each channel at different input wavelengths, the spectral response of each spectral channel of the spectrometer can be obtained and used for the calibration purpose. Figure 6(a) is the calibrated spectral response of the 13 channels (#72 - #84). In this figure, the output of each channel has been normalized to its peak value. The variation of the peaks of the 13 channels is measured to be within ~ 1.5 dB, showing good power uniformity among different channels of the spectrometer. The nonlinear response of the IR camera to different values of the light intensity is not corrected in Fig. 6(a). Therefore, the spectral line shape of each spectral channel is a little broadened in this figure.

The comparison between the extracted resonances from the calibration spectrum and those obtained directly from the through port transmission measurement is shown in Fig. 6(b). A good agreement is observed over the 13 channels under discussion, verifying the reliability of the post-processing method. By fitting the data with a linear function, the average deviation of the cavity resonances from the designed values for this short wavelength range of the 13 adjacent channels is ~ 0.176 nm, a value much smaller than the ~ 0.400 nm obtained for the whole FSR covering 81 channels. We believe the smaller local variation in the resonances of these 13 adjacent spectrum channels is mainly caused by the fabrication imperfections, while the thickness variations of the device layer in the SOI substrate contribute to the larger deviation measured in the long range shown in Fig. 4(b) [19,20].

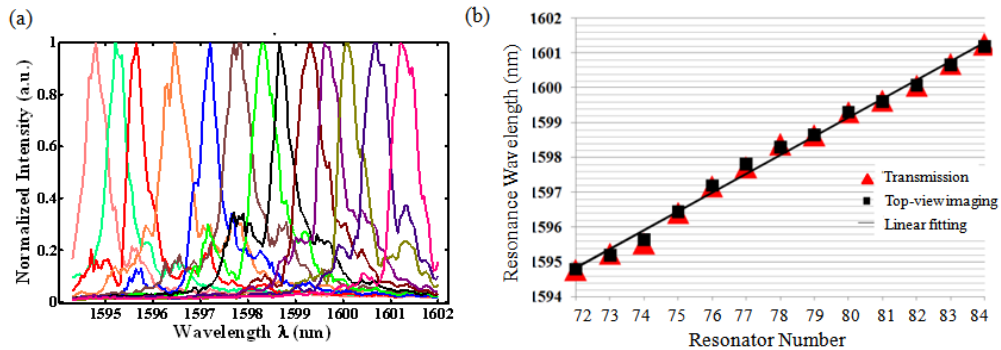


Fig. 6. (a) Calibration spectrum of the 13 channels covering the wavelength range from 1594.30 nm to 1602.00 nm; (b) comparison of resonances obtained by the through port spectrum (triangles) and the calibration spectrum based on the top-view images (squares). A linear model is fitted to the measured resonance wavelengths. The standard deviation of the resonance wavelengths from the linear model is only 176 pm.

5. Discussion

The demonstrated high resolution (~ 0.6 nm) microspectrometer can be very compact thanks to the small size of the miniaturized microdonut resonators and the scatterers. Although the current footprint of this spectrometer is ~ 1 mm², a large portion of the real estate on-chip is occupied by the passive waveguides, which transport the filtered spectral channel signals from the drop port to the scatterer array. Therefore, the size of the spectrometer could be further reduced through suitable optimized device designs for the scatterer array and the drop port waveguides.

One key advantage of the demonstrated spectrometer is the capability of independently controlling and configuring the resolution and the operating bandwidth of each channel of the microspectrometer for different applications. The resolution is well controlled by engineering the coupling between the resonator and the bus waveguide. By implementing different sets of resonator arrays in parallel, the operating bandwidth can be extended to more than one FSR. Ultimately, the spectral range of operation of this microspectrometer is limited by the material absorption of Si as the device layer and SiO₂ as the cladding and buffer layer. Therefore, the proposed spectrometer can cover a wide range of wavelengths from ~ 1.1 μ m to ~ 3 μ m [21]. The main limitation on the spectral resolution is the degree of control on the radii of microdonut resonators. Since the intrinsic Q is very high ($\sim 80,000$ for a 2 μ m radius) and can be further improved by fabrication optimization, the ultimate limit on resolution (assuming full control on the resonator sizes) is very high. This makes the proposed spectrometer a unique device for a wide range of practical applications.

The low insertion loss in this structure not only enables efficient use of the incident optical power, but also maintains uniform power distribution of the signal among different channels, which has been verified by the measured power variation of ~ 1.5 dB. The main challenges are

the shift of the resonances due to the variation of the thickness in the wafer scale and the fabrication imperfections. The former can be solved by further reducing the area of the device. The random variation of the resonator resonant wavelength, caused by fabrication imperfection, impose a challenge, not only in the specific application of high resolution spectrometer as proposed in this paper, but also in many other applications of integrated optics. Different techniques have been proposed for the post fabrication trimming of the integrated optics structure that can reduce these fabrication induced variations and resolve this issue [19,22,23]. Moreover, unlike the case in wavelength demultiplexers, data processing techniques [24] used in the spectrum reconstruction can relax the requirements for the spectral response of the spectrometer. The compatibility of the fabrication processes to the CMOS process enables the integration of these spectrometers with microelectronic and microfluidic circuitry to develop integrated sensing systems for various applications in biological, chemical, medical, and pharmaceutical industries.

6. Summary

In this paper we experimentally demonstrated an 81-channel on-chip spectrometer based on an array of miniaturized microdonut resonators. The single-mode operation of the microdonut resonators with an outer radius of $\sim 2 \mu\text{m}$ enables the large FSR of $\sim 60 \text{ nm}$. The experimental resolution extracted from the calibrated spectral response is $\sim 0.6 \text{ nm}$. The capability of independently engineering the resolution and the operation bandwidth makes the proposed spectrometers suitable for measuring a large range of different target spectra. This high resolution on-chip spectrometer with a large dynamic range shows great potentials as a light weight, compact, high speed, and versatile spectrometer for a variety of applications and for insertion into future lab-on-chip applications.

Acknowledgments

This work was supported by the Defense Advanced Research Projects Agency (DARPA) under Contract No. HR 0011-10-1-0075 and by Air Force Office of Scientific Research under Contract No. FA9550-06-01-2003 (G. Pomrenke).